

# Building Smarter Cities via Intelligent Asset Management: South Carolina Case Study using IBM Maximo Application

Final Report

by

Dr. Paul Ziehl, Ph.D., University of South Carolina  
Office: (803) 467 4030  
Email: [ziehl@cec.sc.edu](mailto:ziehl@cec.sc.edu)

Dr. Nathan Huynh, Ph.D.  
Dr. Gurcan Comert, Ph.D.

November 2023



Center for Connected Multimodal Mobility (C<sup>2</sup>M<sup>2</sup>)



Benedict College



THE CITADEL  
THE MILITARY COLLEGE OF SOUTH CAROLINA

SCState  
UNIVERSITY



UNIVERSITY OF  
SOUTH CAROLINA

200 Lowry Hall, Clemson University  
Clemson, SC 29634

## DISCLAIMER

*The contents of this report reflect the views of the authors, who are responsible for the facts and the accuracy of the information presented herein. This document is disseminated in the interest of information exchange. The report is funded, partially or entirely, by the Center for Connected Multimodal Mobility (C<sup>2</sup>M<sup>2</sup>) (Tier 1 University Transportation Center) Grant, which is headquartered at Clemson University, Clemson, South Carolina, USA, from the U.S. Department of Transportation's University Transportation Centers Program. However, the U.S. Government assumes no liability for the contents or use thereof.*

*Non-exclusive rights are retained by the U.S. DOT*

## ACKNOWLEDGMENT

*The research team greatly thanks C<sup>2</sup>M<sup>2</sup> for partially supporting this project. The SCDOT provided significant support during the development. The report was written with substantial input from the following:*

*Li Ai*

*Laxman KC*

Technical Report Documentation Page

<b>1. Report No.</b>	<b>2. Government Accession No.</b>	<b>3. Recipient's Catalog No.</b>	
<b>4. Title and Subtitle</b> Building Smarter Cities via Intelligent Asset Management: South Carolina Case Study using IBM Maximo Application		<b>5. Report Date</b>	
		<b>6. Performing Organization Code</b>	
<b>7. Author(s)</b> Paul Ziehl, Ph.D. ORCID: 0000-0002-4783-9255 Nathan Huynh, Ph.D. ORCID: 0000-0002-4605-5651 Gurcan Comert, Ph.D. ORCID: 0000-0002-2373-5013		<b>8. Performing Organization Report No.</b>	
<b>9. Performing Organization Name and Address</b> University of South Carolina, 300 Main St, Columbia, SC 29208		<b>10. Work Unit No.</b>	
		<b>11. Contract or Grant No.</b> 69A3551747117	
<b>12. Sponsoring Agency Name and Address</b> Center for Connected Multimodal Mobility (C <sup>2</sup> M <sup>2</sup> ) USDOT Tier 1 University Transportation Center Clemson University 200 Lowry Hall, Clemson, SC 29634		<b>13. Type of Report and Period Covered</b> Final Report (August 2021-November 2023)	
		<b>14. Sponsoring Agency Code</b>	
<b>15. Supplementary Notes</b>			
<b>16. Abstract</b> Over time, bridges experience performance degradation due to factors such as reinforcing steel corrosion, concrete cracks, and declining concrete strength, resulting in a reduced load-bearing capacity. Traditionally, load rating evaluating the safe load-bearing capability of a bridge (expressed as a rating factor) is not only costly but also time-consuming. This process, which can last between 1 to 4 days, often requires lane shutdowns, leading to traffic disruptions. This study introduced a load rating technique leveraging digital twin technology. Data related to crack evolution and inherent strain during loading were obtained by visual inspection of the laboratory bridge slabs using fiber optic strain gauges, acoustic emission sensors, and drones. Subsequently, a calibrated three-dimensional finite element model, representing different loading scenarios, was crafted, forming the foundation for the slab's digital twin. This model was then integrated to represent a segment of South Carolina's Abbeville Bridge, with its accuracy ascertained via field data. Additionally, this research delved into the possibilities of incorporating the digital twin-aided load rating method within Intelligent Asset Management platforms like IBM Maximo. This type of integration may offer a continuously updated virtual bridge model, rich in visual details and informed by real-time monitoring data. Different scenarios can be simulated in the digital twin for predicting the load rating of bridge.			
<b>17. Keywords</b> Digital twin, load rating, Intelligent asset management		<b>18. Distribution Statement</b>	
<b>19. Security Classif. (of this report)</b> Unclassified	<b>20. Security Classif. (of this page)</b> Unclassified	<b>21. No. of Pages</b> 39	<b>22. Price</b> NA

## Table of Contents

DISCLAIMER .....	i
ACKNOWLEDGMENT .....	ii
LIST OF TABLES.....	2
LIST OF FIGURES .....	2
EXECUTIVE SUMMARY .....	1
Introduction .....	2
Literature Review .....	3
1.1 Infrastructure Asset Management using Digital Twin Method .....	3
1.2 Bridge Load Rating.....	7
Methodologies.....	8
1.3 Drone-based Inspection .....	8
1.4 Determination of Health Condition for Load Rating using Drone-based Inspection.....	11
1.5 Investigation of Acoustic Emission .....	14
Results.....	19
1.6 FE Model for a Single Slab.....	19
1.7 Results .....	20
1.8 Investigation 1 .....	21
1.9 Investigation 2.....	23
1.10 Load Rating Procedure Assisted by Digital Twin .....	25
1.11 Integrating the load rating procedure assisted by digital twin with IBM Maximo .....	28
Conclusions .....	30
References .....	31

## LIST OF TABLES

Table 1: Criteria to determine the condition factor. ....11

## LIST OF FIGURES

Figure 1-0-1: Workflow of masonry arch bridge digital twin development (Muhit et al., 2023)..... 4

Figure 1-0-2: Software modules of the digital twin bridge health and structural safety monitoring system (Lei et al., 2022) ..... 5

Figure 1-0-3: Crack visualization method using fiber optic sensors and digital twin (Liu et al., 2023) ..... 6

Figure 2-0-1: Implementation of the CNN Model for load rating..... 8

Figure 2-0-2: The cropped images after image preprocessing (Undamaged) ..... 9

Figure 2-0-3: The cropped images after image preprocessing (Crack) ..... 9

Figure 2-0-4: Images classification using CNN model ..... 9

Figure 2-0-5: Image postprocessing .....10

Figure 2-0-6: Mechanism for grading the condition of bridges .....10

Figure 2-0-7: Slab with cracks .....11

Figure 2-0-8: Images of the slab from a constant height.....11

Figure 2-0-9: Cropping the captured images .....12

Figure 2-0-10: Cropped smaller images .....12

Figure 2-0-11: Implementation of CNN model to obtain images with cracks .....13

Figure 2-0-12: Captured image with bounding boxes .....14

Figure 2-0-13: Merged image of the slab used to estimate the spacing.....14

Figure 2-0-14: Photos of the bending experiments setup .....15

Figure 2-0-15: Load against time schematic and the AE events .....16

Figure 2-0-16: The improved ensemble ANN .....17

Figure 2-0-17: Confusion matrix .....18

Figure 3-0-1: FE model of a single slab: overview of the FE model .....19

Figure 3-0-2: FE model of a single slab: Idealized load vs. time curve .....19

Figure 3-0-3: Modeling results.....20

Figure 3-0-4: Comparison of FE model and experimental results: time vs strain .....20

Figure 3-0-5: Comparison of FE model and experimental results: displacement vs moment .....20

Figure 3-0-6: The two lane bridge (S-97) over Johnson Creek near Abbeville, SC: FE model of one span .....21

Figure 3-0-7: The two lane bridge (S-97) over Johnson Creek near Abbeville, SC: actual bridge .....21

Figure 3-0-8: Dimensions of the bridge span and BDI strain gauges layout .....22

Figure 3-0-9: Truck positions for investigation 1 .....22

Figure 3-0-10: Strain calibration for slab 1 and slab 2 .....23

Figure 3-0-11: Calibration of deflection .....23

Figure 3-0-12: Sensor layout for investigation 2 .....24

Figure 3-0-13: Truck position for investigation 2.....24

Figure 3-0-14: Strain calibration for slab 2.....25

Figure 3-0-15: Displacement calibration for slab 2 .....25

Figure 3-0-16: H20 truck positions .....27

Figure 3-0-17: Operational dashboard of IBM Maximo (IBM 2023).....28

## EXECUTIVE SUMMARY

Due to various factors such as the corrosion of reinforcing steel, cracks in concrete, and a decrease in concrete strength, the performance of bridges diminishes over their service lifespan. Consequently, the load-bearing capacity of bridges typically decreases over time. Load rating is the process of determining a bridge's safe load-carrying capacity, expressed as a rating factor (RF), which is the ratio of the total live load capacity to the weight of the truck used for load rating. In all cases, load rating is a time-consuming and expensive process. Field inspections and load ratings can take between 1 to 4 days, often necessitating lane closures and resulting in traffic congestion. In this project, a load rating method assisted by digital twin technology was developed. A series of strain gauges and acoustic emission sensors were installed on bridge slabs in a laboratory environment to capture crack propagation and existing strains during the loading process. Drone visual inspections were also conducted. A three-dimensional finite element model was created and calibrated based on experimental studies under different loading conditions. Through the calibration of laboratory tests and numerical modeling, a digital twin model of the slab was developed. This slab digital twin model was combined to produce a digital twin model for a span of the Abbeville Bridge in South Carolina and was validated with on-site data. Various loading scenarios were studied to deepen the understanding of the load rating methods for precast reinforced slabs.

Furthermore, this project explored the potential of integrating the developed digital twin-assisted load rating method into the Intelligent Asset Management platform, such as IBM Maximo. IBM Maximo is comprehensive asset management software from IBM. It provides tools and platforms to help businesses manage their physical assets throughout their life cycles, including equipment, infrastructure, facilities, vehicles, and other assets. The aim of Maximo is to help businesses enhance the efficiency and benefits of their assets, thereby reducing operational costs and enhancing the reliability and performance of assets. Integrating the digital twin-assisted load rating into IBM Maximo would allow for the real-time integration of bridge health monitoring data, providing instantaneous health assessments for bridges. Combined with load rating tools, the system could predict the response and performance of bridges under specific load conditions based on real-time monitoring data and advanced analysis models. This serves as guidance for the safe use of bridges. It can also create a virtual model of a bridge, incorporating real-time health monitoring data, offering a highly visual, dynamically updated platform for bridge maintenance and management. In this manner, managers can simulate various scenarios in the digital twin, like different loads or environmental conditions, thereby predicting the actual response of the bridge. From the results of the digital twin load rating, potential maintenance needs are automatically identified, generating maintenance work orders to ensure the bridge remains in optimal condition.



## Introduction

Owing to a variety of factors including the corrosion of rebars, cracks in concrete, and the reduction of material strength, the performance of any bridge inevitably degrades over its operational lifespan. Consequently, the load-carrying capability of bridges typically wanes as time progresses (Islam et al., 2015). Load rating is a procedure to determine the safe load-carrying capacity of bridges, represented by a rating factor (R.F.), which is the ratio of the total live load capacity to the weight of the truck utilized for load classification. However, load classifications are typically time consuming and costly and often require lane closures that result in traffic congestion. Lane closures are necessary not only for the safety of the inspectors, but also due to the need to use large equipment to identify and classify bridge defects. Detecting defects increases the frequency of inspections, which increases costs.

To enhance the efficacy of bridge inspections, it's crucial to augment the objectivity and precision of bridge inspection ratings. Strategies should be devised to mitigate overall inspection costs by eradicating traffic control expenses and reducing labor and equipment outlays. Additionally, there's an imperative need to alleviate safety risks associated with bridge inspection personnel. A paramount objective remains in diminishing the cost and duration of inspections while concurrently maintaining or amplifying the quality of evaluations.

The concept of digital twins in bridge assessments is relatively nascent but presents significant advantages, primarily due to the elimination of extensive instrumentation, specialized loading, and traffic disruptions, thereby effectuating substantial time and resource savings. The feasibility of this method has been bolstered by advancements in data-driven assessment technologies, such as artificial intelligence, and advancements in connectivity. Benefits of this approach encompass the enhancement of mobility for freight (trucks) and other vehicles (like fire trucks, ambulances, and school buses) by potentially reducing bridge replacements or reinforcements, translating into significant cost savings for the SCDOT. Rural communities stand to benefit the most since a majority of load-restricted bridges serve these regions.

## Literature Review

### 1.1 Infrastructure Asset Management using Digital Twin Method

Digital twin method has been utilized in various sectors, notably in infrastructure systems. This section aims to provide an overview of how digital twin advanced asset management in infrastructure systems and to explore the potential of digital twin applied to bridge load rating. In general, digital twin methods rely on advanced sensors, real-time monitoring, and machine learning algorithms.

The synergistic combination of digital twin and sensor monitoring techniques provides multifaceted applications. This integrated approach takes advantage of real-time data collection and computational modeling to provide a comprehensive view of structural integrity. For example, vibration sensors can continuously monitor vibration and motion within an infrastructural component. This real-time monitoring data can be fed into the digital twin model to replicate the physical characteristics and behavior of the infrastructural component in a virtual environment. Mercedes et al. (2022) presented a comprehensive approach to generating seismic fragility curves for a precast reinforced concrete bridge equipped with a vibration-based structural health monitoring (SHM) system, located near an active seismic fault in the Dominican Republic. Given that the bridge serves as a critical lifeline to several local communities and is built to outdated construction standards ill-suited for seismic resilience, the SHM system is essential for assessing its structural integrity and seismic performance. The authors effectively combine data from the SHM system with computational models to produce fragility curves, offering quantitative measurements of expected damage and probabilistic estimates for exceeding various states of failure as functions of seismic intensity. The authors employ a digital twin model of the bridge, developed using finite element analysis and data from the SHM system, as a predictive tool for minimizing modeling uncertainties and enhancing the accuracy of the fragility curves. The proposed digital twin was applied for conducting a nonlinear incremental dynamic analysis (IDA) by utilizing ground motions tailored to the seismic fault and site specifics. The analysis revealed that, considering the highest expected acceleration with a 2% chance of surpassing within 50 years, there's a 62% likelihood of the structure sustaining significant damage.

Lin et al. (2021) presented a novel digital twin-based methodology for assessing the seismic collapse performance of large-span cable-stayed bridges under the influence of strong earthquakes. The study investigated a scaled physical model of a large-span cable-stayed bridge with accelerometer sensors and employs linear and nonlinear model updating techniques to create a digital twin model based on the finite element (FE) model from the original design documents. Subsequently, seismic fragility analysis was performed using the incremental dynamic analysis (IDA) method to generate collapse fragility curves for three different FE models. This paper presents a detailed comparison of the seismic collapse assessments based on these models, scrutinizing their collapse mechanisms, ground motion intensities, and probabilities. These data are then meticulously compared with physical collapse test results to validate the feasibility and accuracy of the proposed digital twin-based approach. The results show that the proposed nonlinear digital twin method is feasible for seismic collapse assessment and superior to the linear digital twin. By comparing the collapse patterns of the from the fragility analysis, only

the nonlinear digital twin is able to provide a consistent and accurate prediction of the bridge collapse pattern under seismic excitation, whereas the linear digital twin is unable to provide a consistent and accurate prediction of the bridge collapse pattern under seismic excitation. Moreover, the linear digital twin cannot correctly predict the damage location of the bridge.

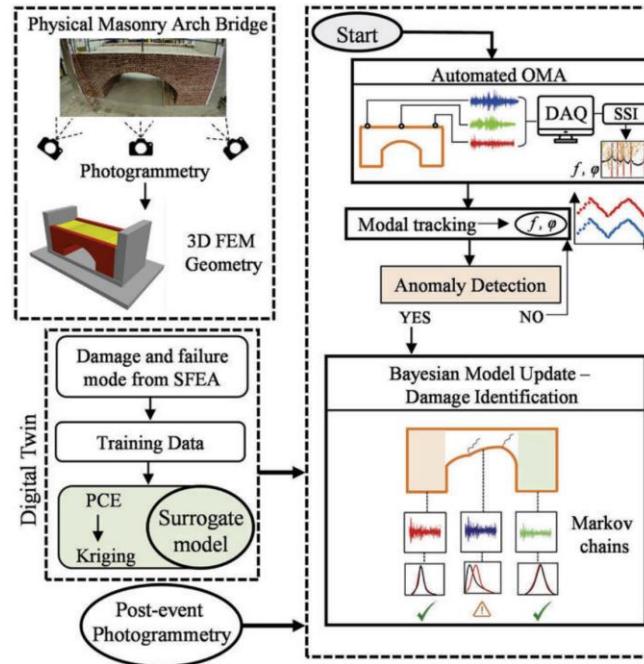


**Figure 1-0-1: Workflow of masonry arch bridge digital twin development (Muhit et al., 2023)**

Muhit et al. (2023) explored the issue of managing Europe aging masonry arch bridges through digital twin. Many bridges in Europe are more than a century old and are subject to operational constraints or closure due to increased traffic loads. The authors introduce a comprehensive framework for creating digital twins of these bridges to facilitate more informed decision-making for their repair and maintenance. The authors elaborate on obtaining dynamic characteristics such as natural frequency and modal shape via ambient vibration tests conducted with accelerometers. A Bayesian approach is used for time-windowed identification of structural modal properties. Combining the photogrammetry-derived 3D geometry with the modal properties, the authors craft a high-fidelity numerical model that can be calibrated continuously using real-world data. This framework has the potential to revolutionize the way aging masonry arch bridges are managed, leveraging advanced real-time monitoring and data-driven approaches to provide condition-based assessments that can significantly improve understanding of damage accumulation over time.

Using Fiber optic sensors can be another way to collect real-time data and update digital twin models. For instance, Febrianto et al. (2022) investigated digital twins incorporating fiber optic strain sensors. Using a case study of a 27.34-meter-long steel railroad bridge in Staffordshire, UK, fitted with fiber Bragg grating sensors at 108 locations, the authors used the statistical finite element method (statFEM) to combine real-world data with a physical based

model, taking into account uncertainties in the sensor readings, applied loads, and model errors. The method provides convincing results that effectively predict the "real" system response in the form of strain distributions on the two main I-girders of the bridge during train passage. The study found that varying the number of sensors (40, 20, 10) and their sampling rates did not significantly affect the precision of the strain predictions of statFEM, as indicated by negligible differences in 95% confidence bounds. This shows that statFEM can reduce the cost of sensor networks while maintaining data interpretability, even if the data set is reduced or incomplete. This suggests that statFEM is capable of generating reasonable strain distribution predictions at points lacking direct sensor measurements, thus expanding its application to long-term structural health monitoring.

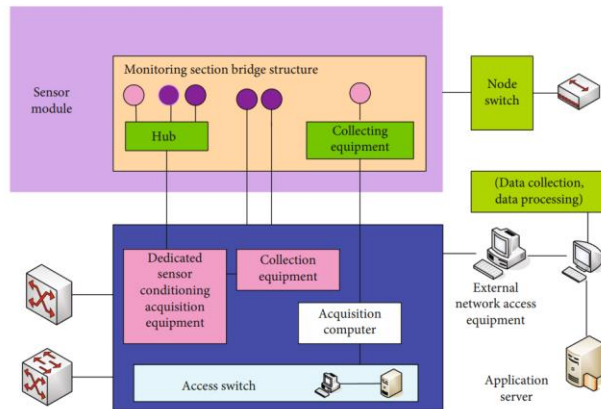
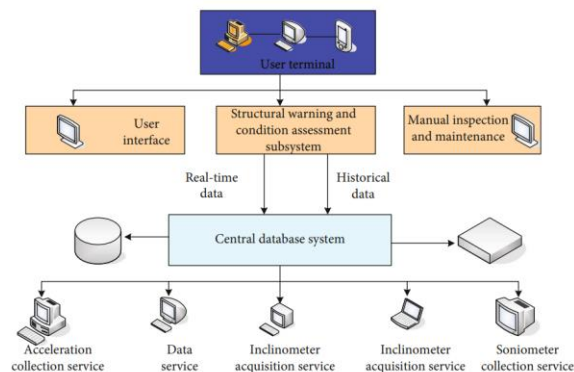


FIGURE 1: Hardware system design of digital twin bridge health structure safety monitoring system.



**Figure 1-0-2: Software modules of the digital twin bridge health and structural safety monitoring system (Lei et al., 2022)**

Lei et al. (2022) presented a digital twin system for the health monitoring of bridges, utilizing a high-speed demodulation system grounded in dual long-period fiber gratings. The study stands out for its fiber grating-based damage self-diagnosis system, which facilitates strain distribution and impact load monitoring. Employing advanced information recognition methods, the system adeptly localizes impact loads. The authors address the inherent challenges of dealing with complex, high-volume data by implementing essential data cleaning techniques, including the transformation of data into dimensionless form and handling missing values. Further, they analyze and construct a digital twin KNN model specifically designed for the monitoring and management of bridge transitions construction. The system architecture is comprehensive,

featuring multiple privilege login modes, a display of BIM models, geographic information, and meteorological data. Additionally, the platform allows for the modification and analysis of data, and even includes email warning functions.

Liu et al. (2023) developed a real-time, updatable digital twin model based on building information modeling. Using machine learning algorithms to intelligently interpret strain distributions, they introduce an automated method for identifying, locating, quantifying, and visualizing cracks that addresses the inefficiencies and inaccuracies of manually interpreting distributed fiber optic sensor data. The model serves as a real-time visualization interface for monitoring cracks, with data continuously provided by distributed fiber optic sensors. The authors validated their method by conducting laboratory tests on concrete beams, achieving highly accurate crack monitoring.

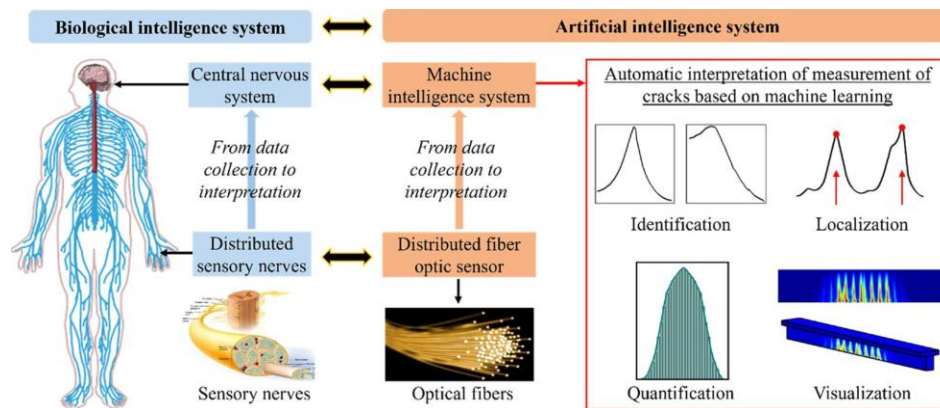


**Figure 1-0-3: Crack visualization method using fiber optic sensors and digital twin (Liu et al., 2023)**

In addition to sensing technologies, drone inspection can be combined with digital twin modeling as it provides accurate and comprehensive information on the health condition of the infrastructure surface. Yoon et al. (2022) developed a digital twin model incorporating drone monitoring in response to the urgent need for periodic inspections of aging bridges. Typically drone inspections usually only map external damage and do not address seismic performance. The authors propose a comprehensive two-phase method that integrates drone-based inspections into a digital twin framework followed by a seismic fragility analysis. This model is updated with bridge conditions sourced from drone inspections, translating observed damage into a quantifiable damage index that reflects reductions in structural stiffness. Using this recalibrated digital twin, the paper runs seismic fragility analyses with varying earthquake scenarios. Their method, tested on an in-service pre-stressed concrete box bridge, demonstrated a notable difference in the seismic fragility curves of a deteriorated bridge compared to an intact one.

Benzon et al. (2022) introduced a method for constructing an operational digital twin for expansive infrastructures, utilizing drone-captured images. Central to this study is the digital twin's capability to virtually mirror the real-world structure and its ability to evolve in tandem with the structure's physical alterations throughout its life span. Validating their approach on a wind turbine transition piece, the authors adeptly harnessed over 500 RGB drone images and multiple LiDAR scans to craft a detailed three-dimensional geometric rendition. This digital construct was then



juxtaposed with the original design to identify and quantify manufacturing inconsistencies and tolerances. Leveraging artificial intelligence, the methodology proficiently identified and categorized paint defects from the images, subsequently mapping them onto the 3D model. This offers the opportunity for real-time updates to the Digital Twin based on periodic inspections. The paper thoughtfully delineates the core technologies underpinning this digital twin concept. Importantly, while the focus here is on wind turbines, the authors emphasize the method's broader applicability across industries like aerospace, marine, transportation, and other substantial infrastructure domains.

## 1.2 Bridge Load Rating

Traditionally, bridge load rating has relied on labor-intensive inspections, manual data collection, and static computational models that require significant time and resources. The current load rating approach is a combination of Diagnostic Load Testing and Proof Load Testing (Lantsoght et al., 2017a,b). Diagnostic load testing measures the response of critical structural components of bridges under specific load test conditions. This may require observations of strain, deflection, or rotation. To analyze these observations, a theoretical model is usually created from reliable data. If the model agrees well with the test results, it can be used to predict the behavior of the structure under a variety of conditions, such as heavy loads or vehicle travel. The key to accurately evaluating bridges by this method is to determine their refined bridge load ratings, which can be derived from design documents, direct measurements, or field material inspections. The methodology discussed is based on testing of similar structures to ensure a reliable understanding of the load-bearing limits of the structure and fine-tuning of the theoretical model based on practical results.

Proof load testing is carried out on bridges with varying loading and unloading in progressively increasing increments to assess their ability to withstand dead and additional live loads. The aim is to apply weights in excess of normal use, provide a safety factor and consider potential dynamic effects. During this process, the response of the bridge is monitored, noting any anomalies or signs of potential damage. While thorough, this method may require the use of heavy vehicles, which can be expensive and disrupt normal traffic. In addition, this method can be risky, especially for certain bridges where failure thresholds may be unclear or easily exceeded. Therefore, the integration of automated methods (e.g., digital twin) is valuable in reliably determining the load-bearing capacity of reinforced concrete bridges, especially those without plans in particular.

## Methodologies

In this section, a drone-based inspection method was developed to determine the health condition factor that is used in bridge load rating. In addition, an ANN was developed to recognize the vehicle loads passing through the bridge using AE sensors.

### 1.3 Drone-based Inspection

The bridges in the substantial inventory of SCDOT have experienced decades of deterioration. When performing bridge load ratings, bridge deterioration is often represented by assigning a condition factor to the bridge slab. This condition factor is determined by bridge inspection. Traditionally, the inspection of bridges has been done by manual visual inspection of the concrete surface. However, this can be costly, labor intensive, and pose a risk to the safety of inspectors. The assessment of bridge conditions also depends on the skills and experience of the inspector. To eliminate these limitations, this study proposes automated bridge inspections. With the development of Unmanned Aerial Vehicle (UAV) technology, drones have been used to construct three-dimensional models for bridge safety inspection, condition assessment, and traffic flow monitoring (Ferozet al., 2021). Drones are used to carry cameras and transmit images to be stored for post-processing in order to monitor the deterioration of bridges. The use of drones helps to reduce budgets, reduce the risk of workplace accidents, and does not disrupt traffic compared to traditional inspection methods (Metni et al., 2007).

An automated inspection framework was developed to detect cracks automatically and estimate the spacing of the cracks in the slab. The condition state of the slab was assigned following the guidelines in the MBEI. Subsequently, a condition factor was determined for the slab, which was used to obtain an updated load rating following the AASHTO MBE standards (AASHTO., 2021). The overall workflow of the framework is illustrated in Figure 2-0-1.

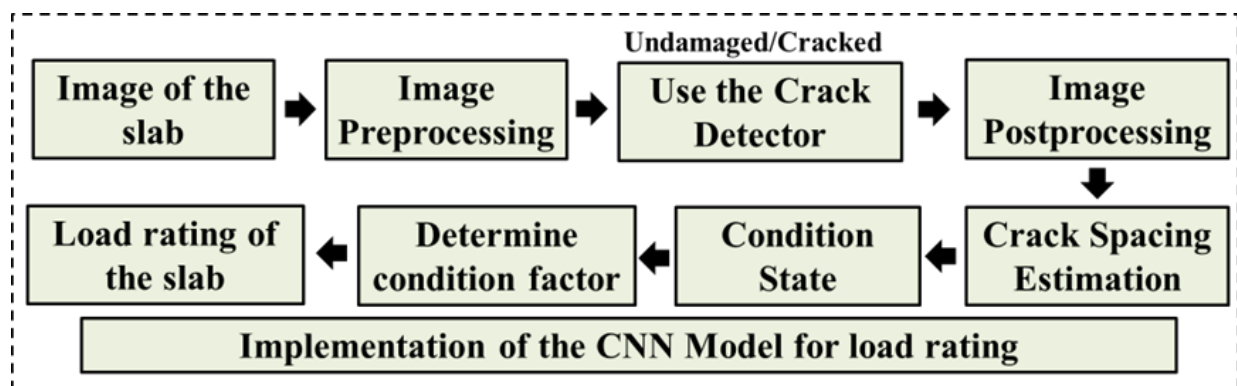
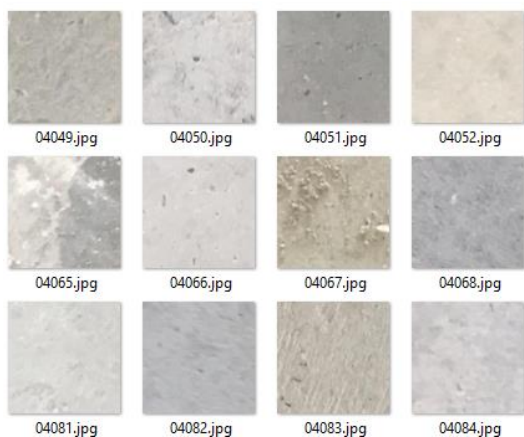


Figure 2-0-1: Implementation of the CNN Model for load rating

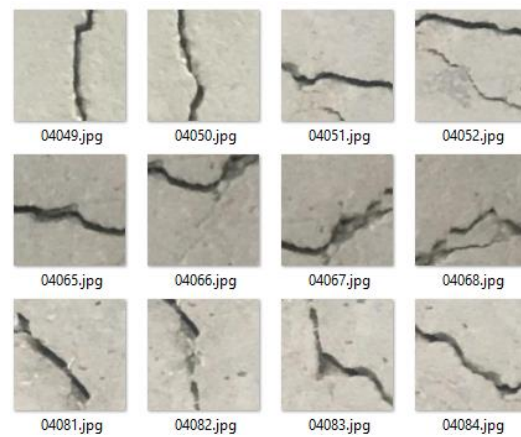
In the automated inspection framework, the acquisition of images is facilitated through the deployment of a drone at a constant elevation. Subsequently, these images are directed towards the image preprocessing module, which plays a crucial role in enhancing their suitability for subsequent analysis. Within this module, the images undergo a transformative operation, namely cropping, resulting in the generation of smaller image segments measuring 64x64 pixels. By segmenting the images into smaller entities, the framework endeavors to facilitate a more granular

inspection and examination of targeted regions of interest, thus enabling more detailed analysis and subsequent decision-making processes.

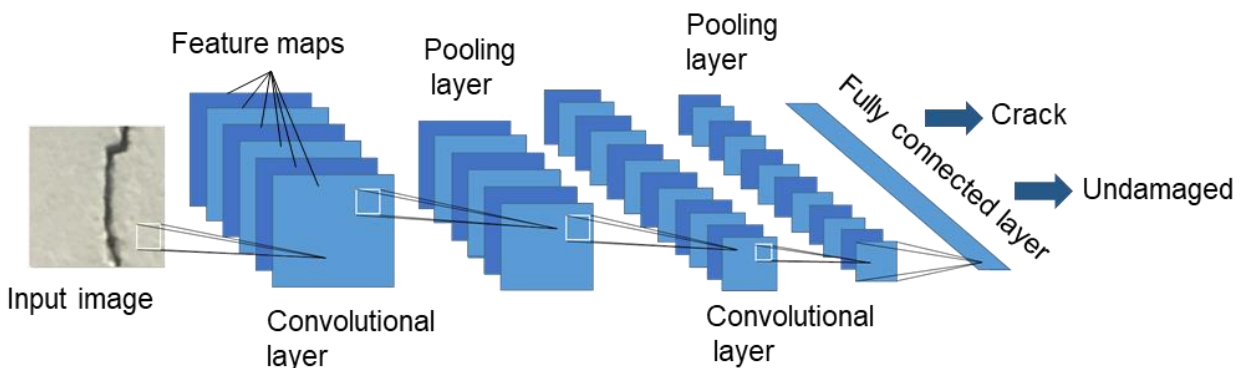
The cropped images after image preprocessing are forwarded to the crack detector which constitutes a pretrained deep learning model encompassing an input layer, a convolutional neural network (CNN) architecture, and an output layer. CNN architecture is used in this project because CNN has performed well in image feature extraction. Through its multilayer structure, CNN is able to effectively recognize and extract complex patterns and features in images, which improves the accuracy and efficiency of the model for tasks such as image recognition, classification, etc. These advantages of CNN make them ideal for processing image data. The development of the CNN model entails training it on a substantial input dataset derived from the ImageNet database, comprising 40,000 images of concrete surfaces. These images are categorized into two distinct sets: those devoid of cracks, denoted as "Undamaged," and those exhibiting cracks, designated as "Crack," as visually represented in Figure 2-0-2 and 2-0-3. Consequently, these images are employed as inputs to the CNN model for the purpose of training and evaluating its performance, as shown in Figure 2-0-4. By employing this approach, the crack detector leverages the comprehensive dataset to learn and identify patterns indicative of cracked concrete surfaces, thereby enabling it to effectively discern between damaged and intact regions during the subsequent inspection and testing phases.



**Figure 2-0-2: The cropped images after image preprocessing (Undamaged)**



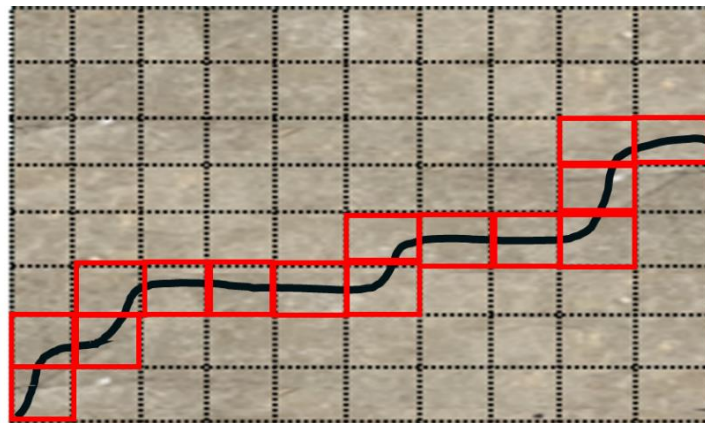
**Figure 2-0-3: The cropped images after image preprocessing (Crack)**



**Figure 2-0-4: Images classification using CNN model**

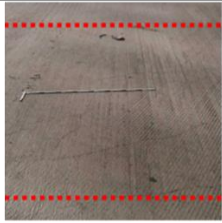




The detector employed in the automated inspection framework provides an output consisting of the cropped images, each labeled as either "Undamaged" or "Crack". The subsequent stage involves the image postprocessing module, which is capable of capturing this output and undertaking the task of reassembling the cropped images, as exemplified in Figure 2-0-5. Notably, in order to visually highlight the presence of cracks, a distinct red box is assigned to each cropped image labeled as "Crack." When multiple instances of the "Crack" labeled images are detected in close proximity, these red boxes are interconnected to form a continuous crack path, allowing for a comprehensive representation of the damaged areas. Moreover, by measuring the number of pixels that separate these crack paths, it becomes feasible to estimate the distance between two cracks.



**Figure 2-0-5: Image postprocessing**

Once the distance of the cracks is automatically estimated, the condition factor  $\emptyset_c$  can be determined. The Bridge Component Inspection Manual provides a systematic assessment of the structural integrity of concrete bridges, focusing on the occurrence and spacing of surface cracks. Figure 3.5 provides a mechanism for grading the condition of bridges, specifically for the spacing between concrete surface cracks in bridges. This spacing is an important indicator of potential structural deterioration. The table is categorized into three states: 'Condition State 1', 'Condition State 2', and 'Condition State 3'. Status 1 (good) indicates that crack spacing exceeds 3.0 feet, indicating a minor structural problem. Conversely, Status 3 (poor) refers to crack spacing of less than 1 foot, indicating a serious structural problem.

Defects	Condition State 1	Condition State 2	Condition State 3
Cracking	 <p>Spacing greater than 3.0 ft.</p>	 <p>Spacing of 1.0—3.0 ft.</p>	 <p>Spacing of less than 1 ft.</p>

**Figure 2-0-6: Mechanism for grading the condition of bridges**

The condition factor  $\emptyset_c$  can be determined following the Specifications for the National Bridge Inventory, as shown in Table 1 This coefficient assigns values to the previously discussed

condition states: 'good', 'fair' and 'poor'. State 1 (good) corresponds to a condition coefficient of 1.00, indicating that the structure is in optimal condition with negligible defects. Status 2 (fair) has a status coefficient of 0.95, indicating a generally acceptable condition with minor defects. Status 3 (poor) with a status coefficient of 0.85 indicates that the structure has serious defects or deterioration that may threaten its overall integrity.

**Table 1: Criteria to determine the condition factor.**

Equivalent member structural condition	Condition Factor ( $\phi_c$ )
CS 1 (Good)	1.00
CS 2 (Fair)	0.95
CS 3 (Poor)	0.85

#### 1.4 Determination of Health Condition for Load Rating using Drone-based Inspection

To automatically detect and estimate the spacing of cracks on a slab (Figure 2-0-7), a drone was employed to capture images of the slab. Three strategic points on the slab were selected, ensuring coverage of the entire surface area. At a constant height, the drone captured images from these points as shown in Figure 2-0-8. These three images were then utilized to automate the estimation of crack spacing.

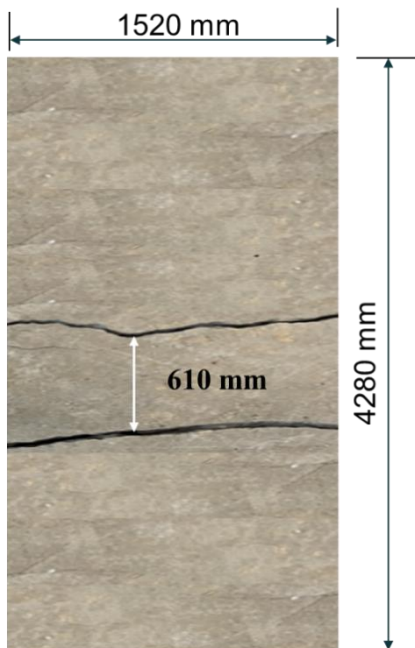


**Figure 2-0-7: Slab with cracks**

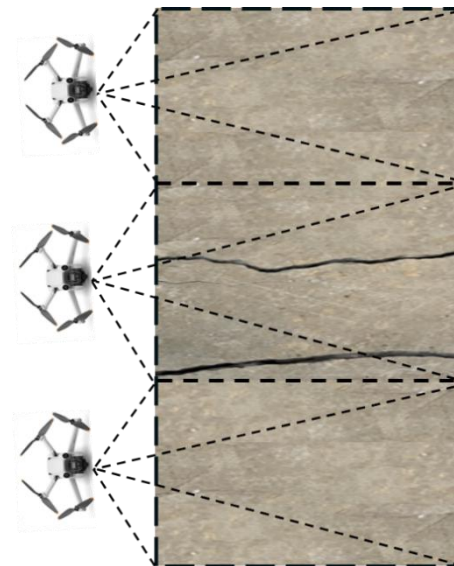


**Figure 2-0-8: Images of the slab from a constant height**

To ensure a thorough examination of the slab, a systematic approach was employed, involving the capture of three high-resolution images from a consistent height of 914 mm. Each of these images possessed dimensions of 512x320 pixels, enabling a detailed representation of the inspected area. To facilitate efficient analysis and maintain uniformity throughout the

inspection process, a subsequent step involved the cropping of these captured images into smaller segments, measuring 64x64 pixels. The rationale behind this cropping process is elucidated in Figure 2-0-9 and 2-0-10, which visually illustrates the procedure for cropping both the original captured images and the resulting smaller segments. The decision to adopt this specific size was guided by the objective of preserving the accuracy of the binary-class convolutional neural network (CNN) model, which had been trained on images with an identical number of pixels. By ensuring consistency in the dimensions of the images, it was anticipated that the performance and accuracy for detecting cracks would remain reliable. This deliberate choice aimed to minimize potential distortions or inconsistencies that could arise from variations in image sizes, thereby maximizing the effectiveness of the trained CNN model in accurately identifying cracks within the inspected concrete surfaces.

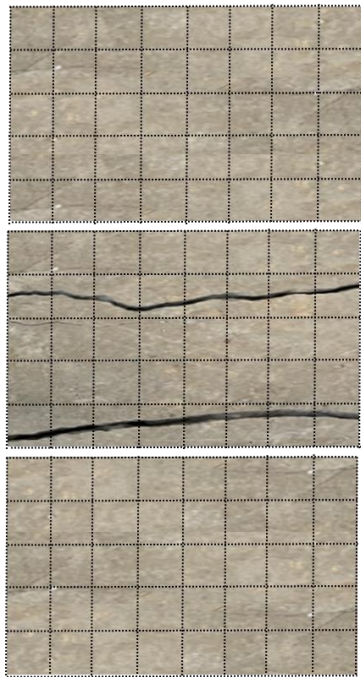


**Figure 2-0-9: Cropping the captured images**



**Figure 2-0-10: Cropped smaller images**

Following the process of cropping the captured images into smaller dimensions of 64x64 pixels, the resulting segmented images were subjected to the trained CNN model. The primary objective was to leverage the sophisticated capabilities of the CNN model in accurately identifying the presence of cracks within the images. Figure 2-0-11 displays the images that were classified as "Cracked," thereby visually illustrating the successful identification of these cracked areas.

Subsequently, the cropped images were amalgamated to reconstruct the original individual captured image. To visually emphasize the detected cracks, bounding boxes were superimposed onto the corresponding images classified as "Cracked." This visual representation is presented in Figure 9a. The aforementioned procedure was repeated for the second and third images of the slab, wherein each image was individually cropped, fed into the CNN model, and scrutinized for crack detection. The resulting cracked regions were visually highlighted by applying bounding boxes to each respective image, facilitating a clear identification of the areas exhibiting damage.

Upon successfully processing all three images, the subsequent step involved merging them to generate a unified and comprehensive depiction of the entire slab. By combining the three processed images, a singular cohesive image of the entire slab was created, as demonstrated in Figure 2-0-13. Importantly, the bounding boxes that demarcated the cracked regions within each individual image were retained in the final unified image, ensuring a visually explicit reference to the identified cracks. This comprehensive image representation serves as a valuable visual aid for an accurate assessment of the condition of the inspected slab, enabling stakeholders to make informed decisions regarding necessary repairs and maintenance interventions.

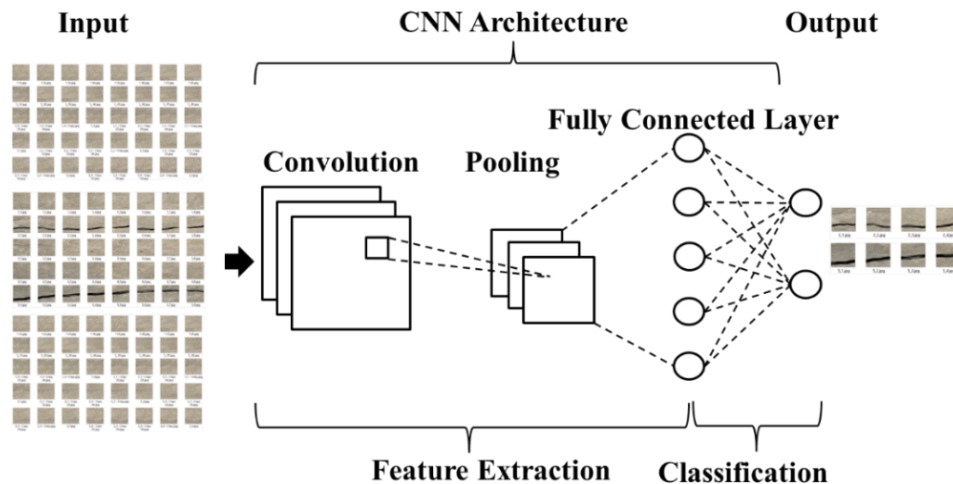


**Figure 2-0-11: Implementation of CNN model to obtain images with cracks**

To estimate the spacing between the cracks, the pixels between the images with bounding boxes on the same column were obtained. The minimum value of the pixel was estimated to be the spacing between the cracks. The pixel value was then multiplied with the scale factor in the vertical direction to obtain the spacing between the cracks. Based on the estimated spacing, a condition state was assigned to the slab according to the guidelines in the MBEI. The assigned condition state was utilized to determine a condition factor, following the guidelines outlined in the AASHTO MBE. This condition factor accounts for the structural condition of the slab and is used in updating the load rating for an accurate evaluation of the slab's load-carrying capacity.



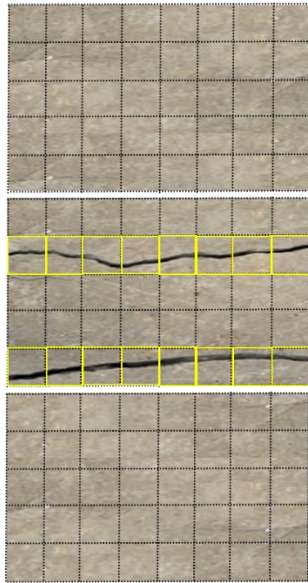


**Figure 2-0-12: Captured image with bounding boxes**

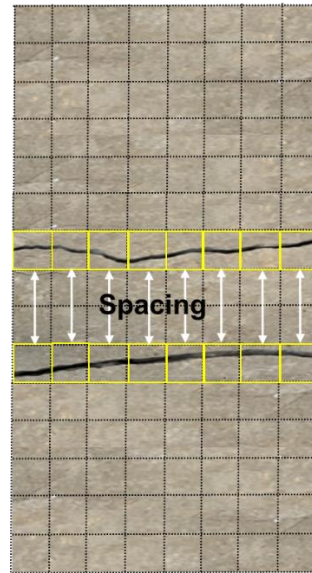


**Figure 2-0-13: Merged image of the slab used to estimate the spacing**

During the manual visual inspection of the slab, a spacing of 610 mm was measured between the cracks. This spacing falls within the range of 305 mm to 914 mm. As per the guidelines in the MBEI, the condition state assigned to the slab based on this visual inspection is Condition state 2. Accordingly, a condition factor of 0.95 would be assigned to the slab for load rating purposes.

Upon implementing the CNN model, a minimum pixel value of 128 was obtained from the crack detection process. To convert this pixel value into a physical spacing, a scale factor of 4.40 mm/pixel was calculated. This scale factor was determined based on the length of the slab and the total number of pixels in the vertical direction. Utilizing the scale factor, the minimum pixel value of 128 was converted, resulting in an estimated spacing of 563 mm between the cracks after implementing the model. Since this spacing also falls within the range of 305 mm to 914 mm, the assigned condition state remains the same as Condition state 2, consistent with the visual inspection results.

Consequently, the condition factor of 0.95, which was initially assigned based on the visual inspection, is retained for the load rating of the slab. The implementation of the model yielded a comparable estimation of crack spacing and confirmed the condition state and condition factor determined through visual inspection.

## 1.5 Investigation of Acoustic Emission

This chapter also investigated Acoustic Emission (AE), as a vehicle load determination method to assist load rating. Bending experiments were executed on a precast RC flat slab supplied by SCDOT, intending to replicate the stresses exerted by vehicles traversing bridges. This slab, having served as part of a bridge for at least three decades, was later stored at an SCDOT establishment. The dimensions of these slabs were 15 feet in length, 8.25 inches in thickness, and 5.5 feet in width. The typical reinforcement specifications comprised No. 7 bars spaced at 6-inch intervals longitudinally and No. 4 bars spaced at 12-inch intervals transversely. The compressive strength of concrete and the yield strength of steel bars stood at 4,000 psi and 60,000 psi, correspondingly. To exert force, a hydraulic actuator was employed, while a load cell

monitored the force values. A steel dispersing beam was placed at the mid-point of the slabs, between the hydraulic actuator and the sample (refer to Fig. 2-0-14). A four-point bend setup was achieved by introducing neoprene cushions between the actuator and the dispersing beam. This loading scheme mirrors the AASHTO HL-93 design tandem, featuring a 4-foot axle distance (AASHTO., 2021), inducing the maximum consistent moment in the slabs. The test configurations are depicted in Figure 2-0-14.

The load exerted on the slabs followed a progressive cyclic pattern. The initial load was set to 2 kip. Subsequently, it elevated to 10 kip, maintained, and then reduced back to 2 kip, labeled as load step 1 (L1). Then, the force rose to 20 kip, sustained, and reverted to 2 kip, denominated as load step 2 (L2). Finally, the slab endured a load of 30 kip, held, and returned to 2 kip, termed as load step 3 (L3). The load against time schematic for these tests can be observed in Figure 3.11. The rationale for designing load steps 1 to 3 was to emulate the probable vehicular weights these slab infrastructures might bear over their operational lifespans.

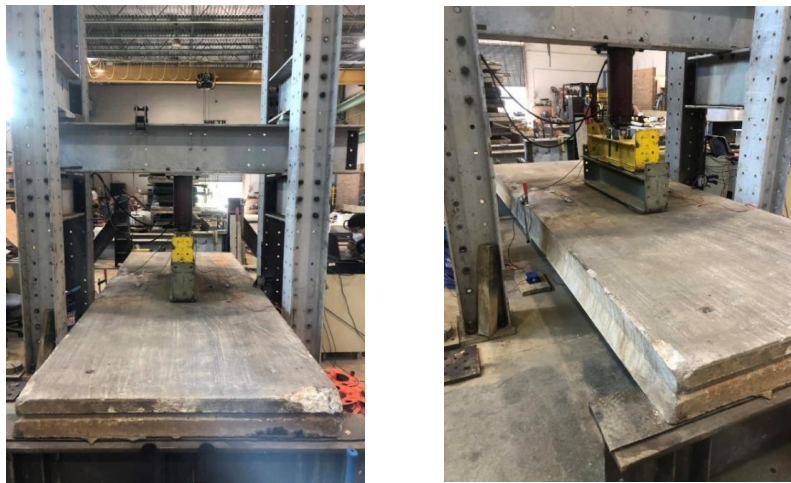


**Figure 2-0-14: Photos of the bending experiments setup**

Data on acoustic emission was gathered employing the Sensor Highway II data acquisition platform in conjunction with four broadband sensors of type WDI. The choice of broadband sensors was influenced by their superior frequency operational range in comparison to resonant AE sensors. These sensors possess a functional frequency spectrum spanning from 100-900 kHz. Such a broad spectrum assures the proficient capturing of the response across varying frequencies. To validate the responsiveness of the WDI sensors, an attenuation assessment utilizing the Hsu-Nielsen pencil lead break method was executed. The outcomes corroborated the capability of sensor to discern signals even from the most distant points on the specimen surface. As delineated in Fig. 2-0-15, the sensors were strategically positioned at intervals of  $L/3$  and  $W/3$  across the longitudinal and transverse axes, respectively. To affix the sensors to the specimen, a double/bubble epoxy adhesive was employed.

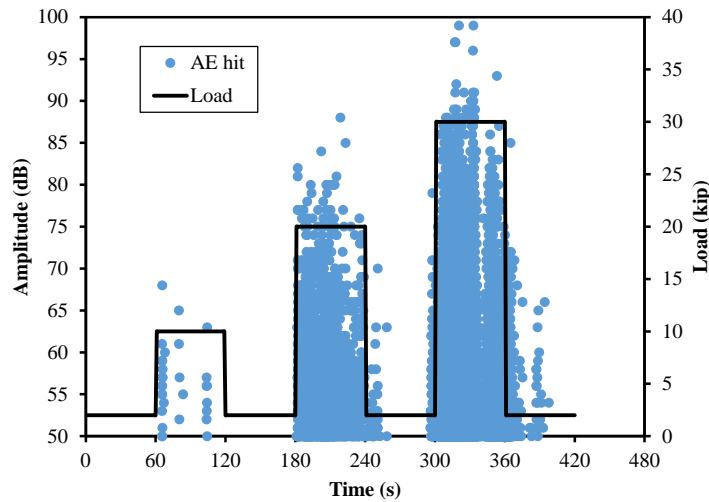


**Figure 2-0-15: Load against time schematic and the AE events**

Given the outstanding performance of Artificial Neural Networks (ANN) in previous research on acoustic emission signal processing (Ai et al., 2021a, Ai et al., 2021b, Ai et al., 2021c) an ANN was employed in this chapter to categorize AE events based on their associated AE characteristics, correlating them with specific vehicle loads. During the ANN training phase, an imbalance emerged, with data points from load step 3 significantly outnumbering those from load step 2 at a ratio of roughly 10:1. To mitigate this disparity, an improved ensemble ANN algorithm (as shown in Figure 2-0-16) was developed that fractionated the data from load step 3 into ten distinct subsets. Subsequently, ten distinct models were cultivated using data from load step 2 combined with a fraction (one-tenth) of the data from load step 3. Each of these models underwent testing against a randomly chosen set from both load steps 2 and 3. The aggregated decisions from all models, based on a majority voting mechanism, determined the final categorization of each data point.

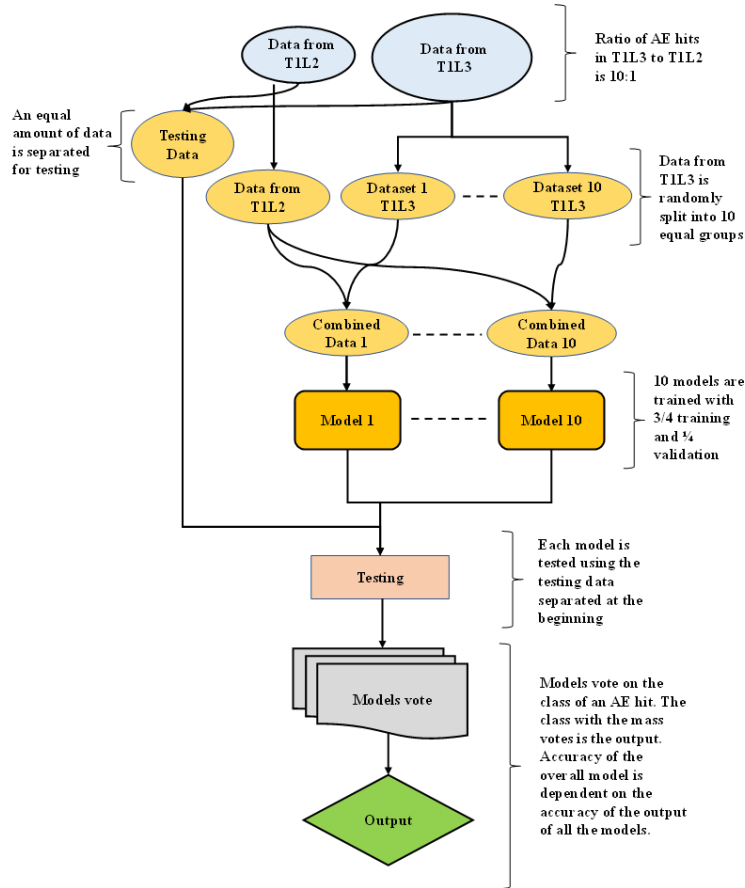


**Figure 2-0-16: The improved ensemble ANN**

The improved ensemble ANN exhibited a commendable recall of 90.5% for step 2 classification, accurately classifying 410 out of 453 AE events. For step 3 classification, it achieved a recall rate of 81.2%, correctly categorizing 342 out of 421 AE events. The model showcased an aggregate accuracy of 86.0%, rightly categorizing 752 out of 874 AE events. Notably, while the model's comprehensive accuracy declined by 4.8%, the recall for T1L2 surged by an impressive 65.3% due to the harmonized training data across both steps 2 and 3. This illustrates the model's enhanced capability in distinguishing events from both steps 2 and 3. The corresponding confusion matrix for this model is depicted in Figure 2-0-17.



		<b>Recall</b>		
		T1L2	T1L3	
<b>Actual Load Step</b>	T1L2	410	43	90.5%
	T1L3	79	342	81.2%
<b>Precision</b>		83.8%	88.8%	86.0%
		T1L2	T1L3	
		<b>Predicted Load Step</b>		

Figure 2-0-17:Confusion matrix

## Results

In this chapter, the finite element model of a span from the bridge in Abbeville, SC is constructed using ABAQUS. This model comprises four individual slabs that are assembled to represent the entire span. Before delving into the details of the span model, it's essential to discuss the individual slab models (Figure 1).

### 1.6 FE Model for a Single Slab

For the slab, 8-node C3D8R elements were employed, while the rebar utilized 2-node B31 elements. The mesh size for the concrete was consistently maintained at a 1-inch cubic dimension. In terms of material properties, Young's modulus for the steel rebar was set at 29,000,000 psi. In contrast, the concrete's Young's modulus was set as 3,605,000 psi. The slab model was calibrated using a four-point bending test. The overview of the slab model and the applied load during the test can be viewed in Figure 3-0-1 and 3-0-2. To emulate a real-world scenario of a vehicle crossing, step loads of 10kips, 20kips, and 30kips were applied. After applying the step load, another load was also applied to the slab up to failure.

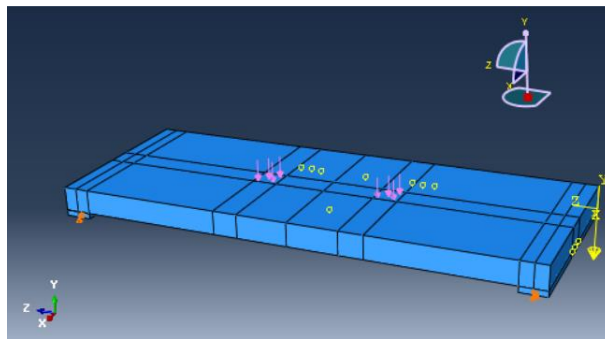


**Figure 3-0-1: FE model of a single slab: overview of the FE model**

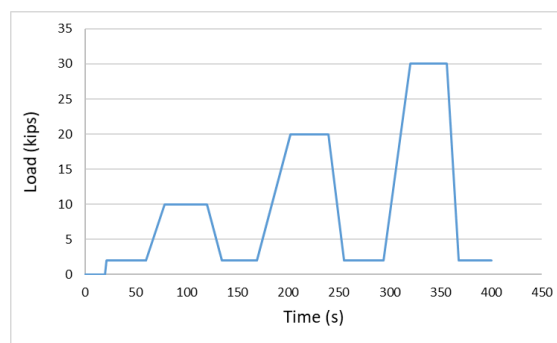


**Figure 3-0-2: FE model of a single slab: Idealized load vs. time curve**

Following the application of the load as depicted in the figure, the von Mises stress results from the FE model are presented in Figure 3-0-3. A comparison was made between the time-strain curves under step load provided by the FE model and those from the experiments, as shown in Figure 3-0-4. It is evident that the trend of the FE model is reasonably consistent with the experimental results. Additionally, a comparison was drawn between the moment versus midspan

displacement curve from the FE model and the experimental data, as shown in Figure 3-0-5. The yielding moment of the slab, as determined from the FE model and the experiments, is 228 ft-kips and 211 ft-kips respectively. The ultimate moment of the slab, as derived from both the FE model and the experiments, is 247 ft-kips and 254 ft-kips respectively. These comparisons underscore the capability of the finite element model to simulate the elastic phase and the yielding up to the failure phase of the slab.

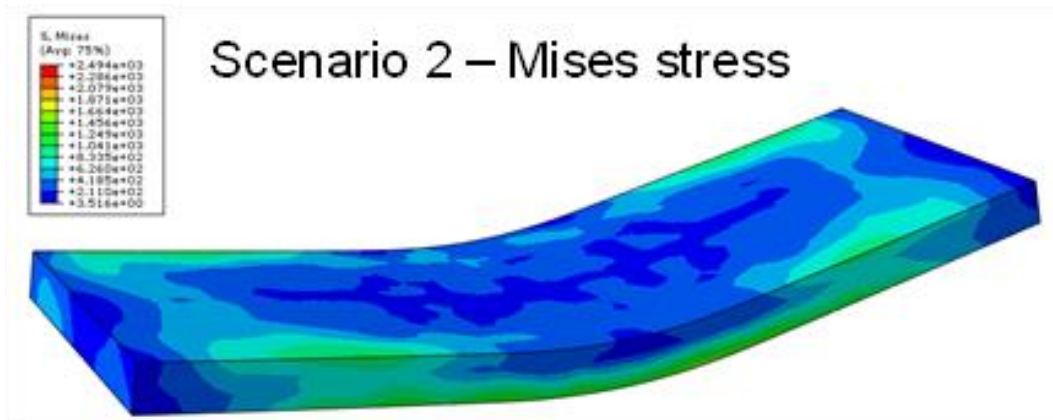


Figure 3-0-3: Modeling results

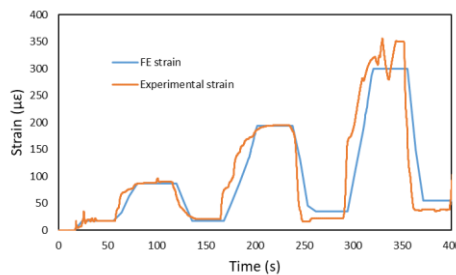


Figure 3-0-4: Comparison of FE model and experimental results: time vs strain

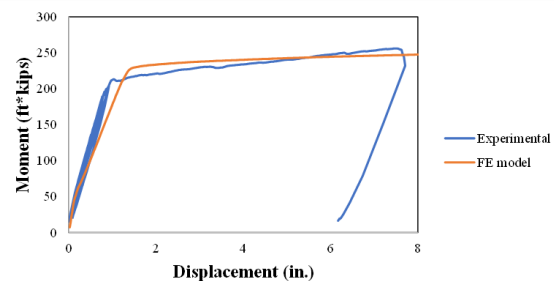
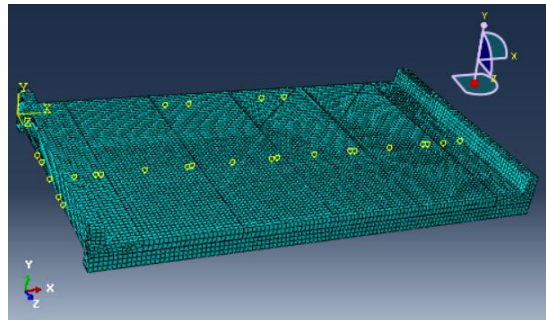


Figure 3-0-5: Comparison of FE model and experimental results: displacement vs moment

## 1.7 Results

Upon the completion of the calibration of the slab model with experimental data, four such slab models were assembled to form a model representing a bridge span. The model is depicted in Figure 3-0-6. This model was calibrated based on two investigations. Investigation 1 was introduced in a previous report (Ziehl et al., 2020). Investigation 2 was conducted on May 16<sup>th</sup>, 2023. Both investigations 1 and 2 were conducted on a two lane bridge (S-97) over Johnson Creek near Abbeville, SC (Figure 3-0-7). The bridge was built in 1959 and was designed as an

eight-span bridge. Each span of the bridge consists of four interior and two exterior panels (flat slabs with 9.25 in (0.23 m) thickness) supported by reinforced concrete pier caps and timber piles.



**Figure 3-0-6: The two lane bridge (S-97) over Johnson Creek near Abbeville, SC: FE model of one span**



**Figure 3-0-7: The two lane bridge (S-97) over Johnson Creek near Abbeville, SC: actual bridge**

## 1.8 Investigation 1

In Investigation 1, strain gauges and potentiometers were positioned and secured to monitor deformation effects during loading. Real-time strain measurements were recorded as the trucks drove past specific locations (locations 1 through 3). The layout of the strain gauges potentiometers is shown in Figure 3-0-8, These measurements were compared to the strain values predicted by the FE span model, which served as a key reference point. To get a clearer picture of the truck's movement and positioning during this phase, a detailed schematic of the truck's positions (from 1 to 3) is provided in Figure 3-0-9.

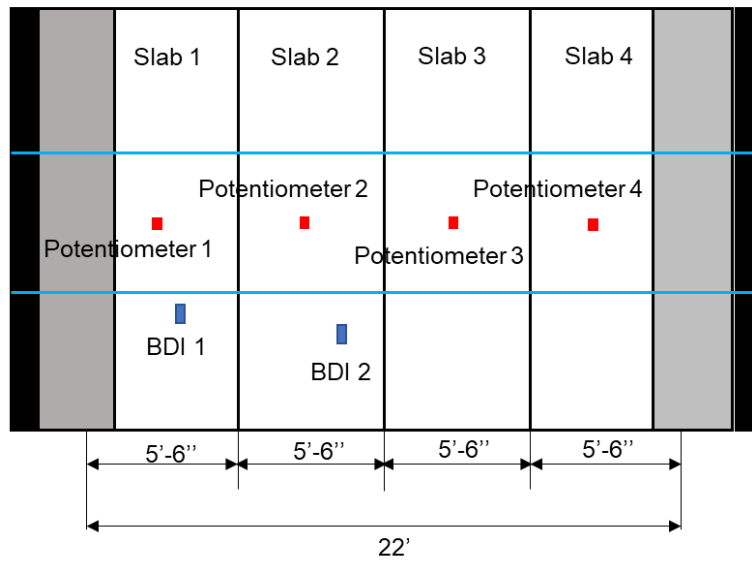


**Figure 3-0-8: Dimensions of the bridge span and BDI strain gauges layout**

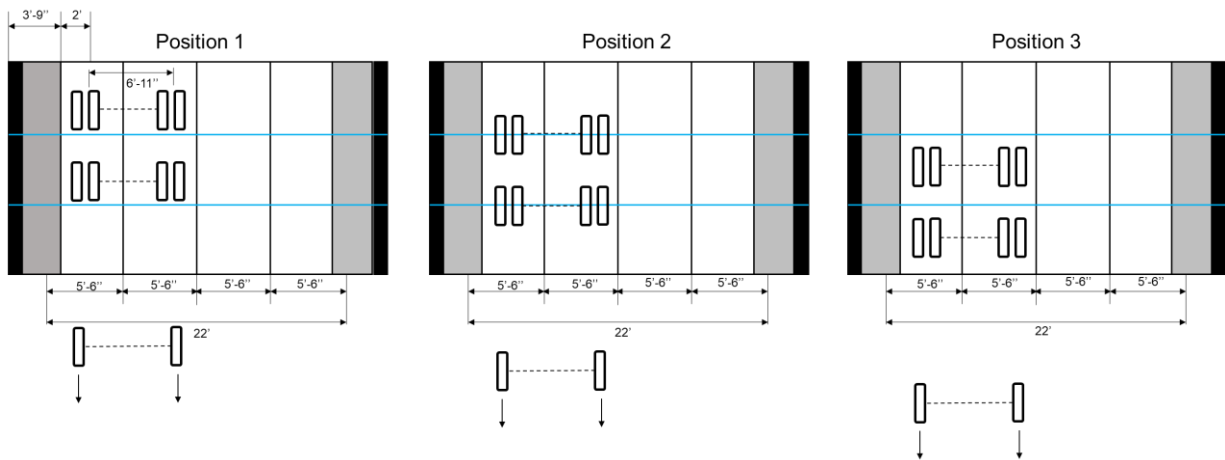


**Figure 3-0-9: Truck positions for investigation 1**

Although there were slight differences, the strain readings from the FE model for the bridge span at three distinct truck placements were in strong agreement with the actual measurements taken from the bridge span, as illustrated in Figure 3-0-10. Additionally, when comparing the peak deflection of each slab in the FE span model, it closely resembled the deflection observed in the slabs of the actual bridge, as represented in Figure 3-0-11. This resemblance indicates that the model effectively mirrors the load distribution across the slabs in the real bridge span.

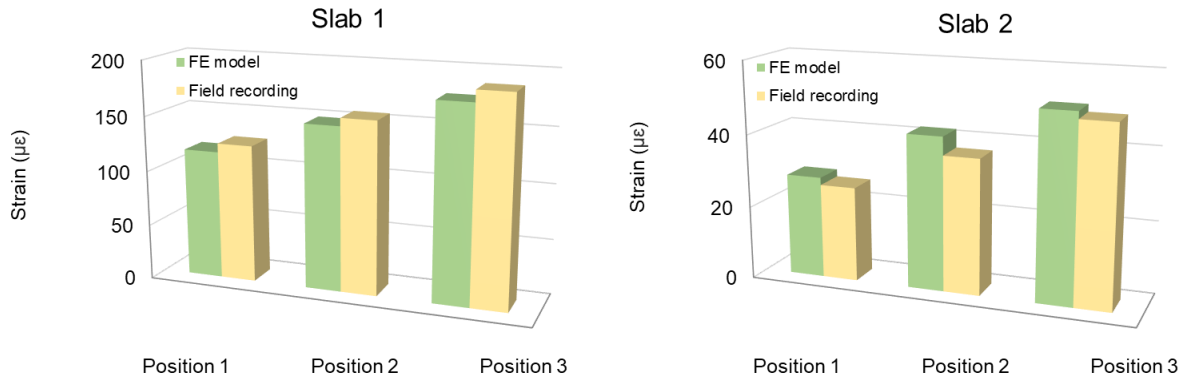


**Figure 3-0-10: Strain calibration for slab 1 and slab 2**

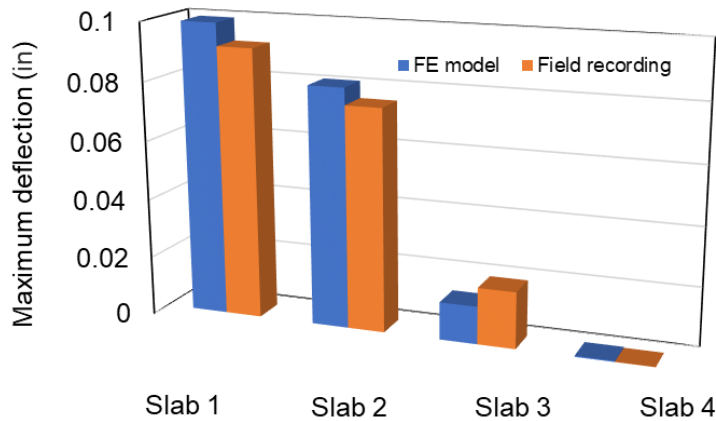


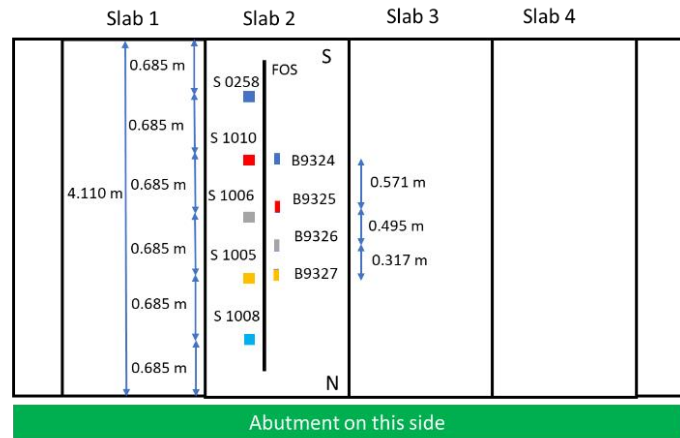
**Figure 3-0-11: Calibration of deflection**

### 1.9 Investigation 2

In Investigation 2, potentiometers, BDI strain gauges, and optical fiber sensors were employed. The placement of these sensors is depicted in Figure 3-0-11. In the context of Investigation 2, the positioning of truck differed from that of Investigation 1. The specific truck position is illustrated in Figure 3-0-12. The truck load assigned to each axle is 7.5kips.



Sensors on the bottom of the slab 2



Schematic showing BDI strain gages on the bottom of the slab 2

Note: S: String potentiometer FOS: Fiber Optic Sensor B: BDI strain gage

**Figure 3-0-12: Sensor layout for investigation 2**

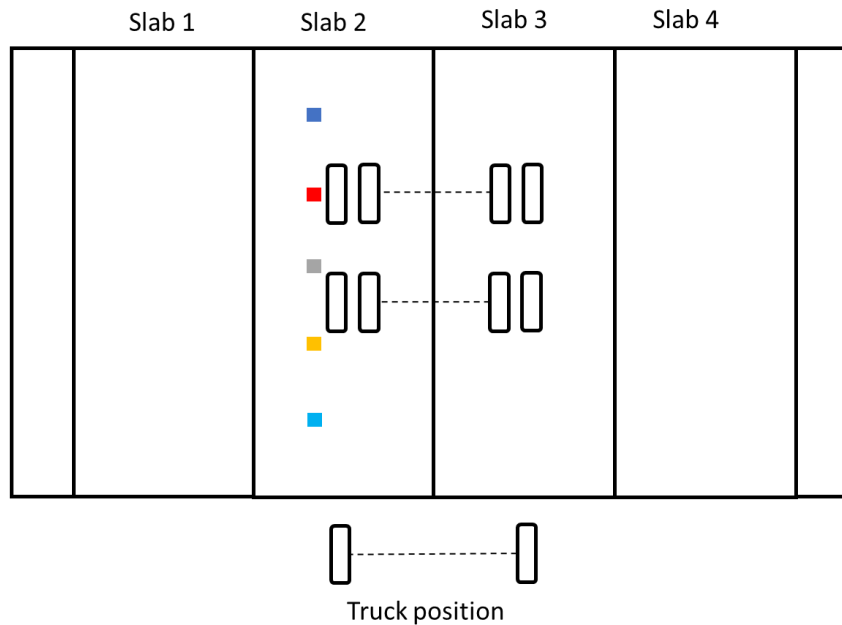


**Figure 3-0-13: Truck position for investigation 2**

Figure 3-0-14 presents a comparative analysis of the strain data derived from the fiber optic sensor, the BDI strain gauge, and the FE model. Notably, the FE model's strain predictions align closely with the measurements taken by the fiber optic sensor. Similarly, Figure 3-0-15 displays a comparison between the displacement data gathered from the fiber optic sensors, potentiometers, and the FE model. The FE model's displacement estimates are observed to be in close agreement with the readings from the potentiometers.

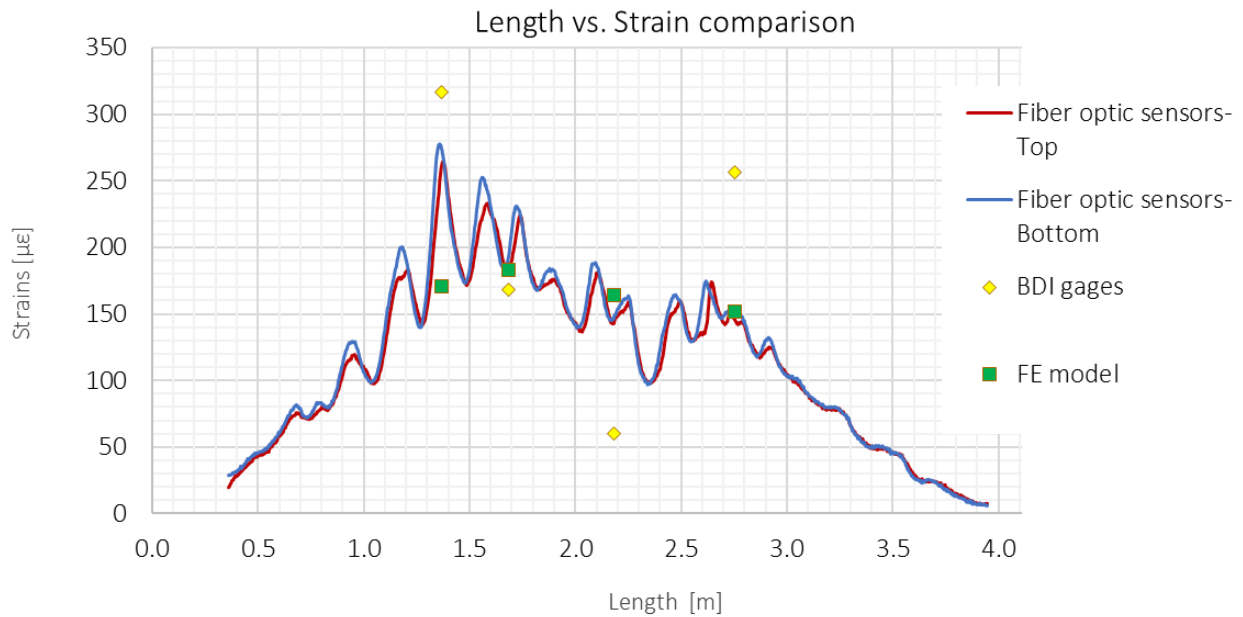


**Figure 3-0-14: Strain calibration for slab 2**

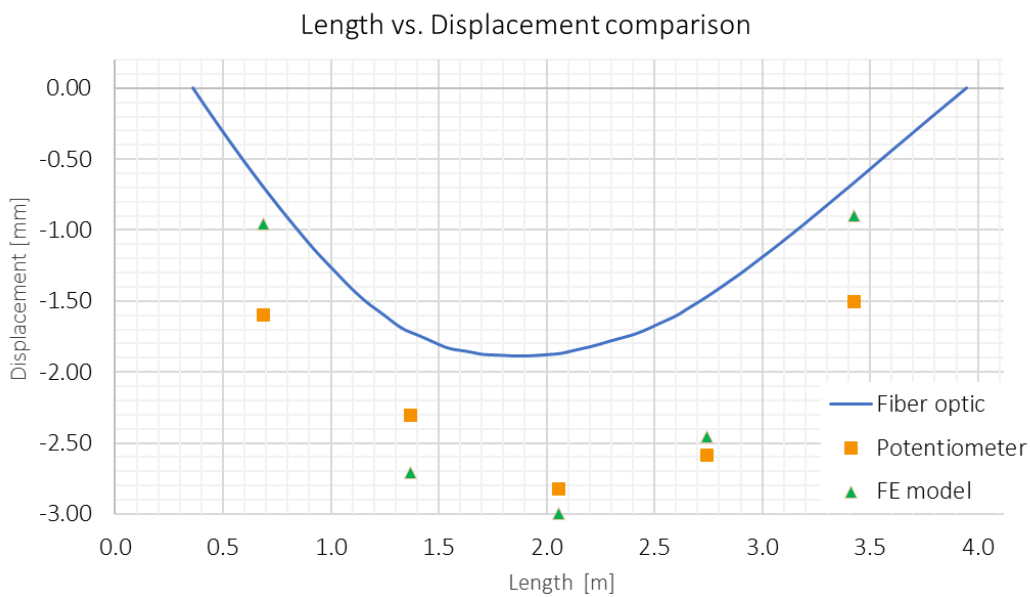


**Figure 3-0-15: Displacement calibration for slab 2**

### 1.10 Load Rating Procedure Assisted by Digital Twin

A method for load rating assisted by a digital twins model was proposed for the dual-lane bridge as mentioned before. This bridge was outfitted with strain gauges, potentiometers, and fiber optic sensors to gauge its behavior under traffic-induced loads. A Finite Element (FE) model of the bridge's span was created and calibrated with data gathered from the actual bridge.

For standard load rating practices in South Carolina, the Load and Resistance Factor Rating



(LRFR) equation (SCDOT 2019) was utilized to calculate the load rating factor of the bridge's flat slabs, as outlined in Eq. (1).

$$RF = \frac{\phi_c \phi_s \phi R_n - \gamma_{DC} D_C - \gamma_{DW} D_w}{\gamma_L L (1 + IM)} \quad (1)$$

where  $RF$  is the load rating factor,  $\phi_c$  is the health condition factor of the flat slab being load rated,  $\phi$  is the LRFD resistance factor,  $R_n$  is the nominal member resistance which refers to the ultimate moment capacity,  $\gamma_{DC}$  is the permanent load factor for bridge components,  $D_C$  is the permanent load effect,  $\gamma_{DW}$  is the dead weight factor for the wearing surface,  $D_w$  is the dead load effect of the wearing surface and utilities,  $L$  is the live load effect of an AASHTO vehicle,  $IM$  represents the dynamic amplification, and  $\gamma_L$  denotes the live load factor. The analysis did not account for the wearing surface and utilities, hence  $\gamma_{DW}$  and  $D_w$  were excluded from consideration.

The report introduces an innovative method for load rating using a digital twins approach. This method involves a new equation for calculating the load rating factor, which is distinct from traditional methods. The equation is presented as Eq. (2):

$$RF = \frac{\phi_c \phi_s \phi R_{n-FE} - D_C - D_w}{\gamma_L L_{FE} (1 + IM)} \quad (2)$$

Where,  $R_{n-FE}$  is used to describe the maximum moment capacity ascertained by the model, while  $L_{FE}$  refers to the live load impact determined through the same model.

Traditional methods for load rating typically calculate the live load effect, symbolized as  $L$ , by factoring in vehicle load and its distribution. However, the updated approach involves deriving  $R_{n-FE}$  from a FE model of a single slab, which is calibrated using experimental data. Similarly,  $L_{FE}$  is computed utilizing the FE model for the bridge's span. The modification of the LRFR equation aims to diminish the influence of variables like the permanent load factor, as the dead load can be more precisely estimated based on the dimensions and density of the concrete.

This recalibrated FE span model was then applied to perform a load rating for an H20 truck, using the truck positioning illustrated in Figure 3-0-16.

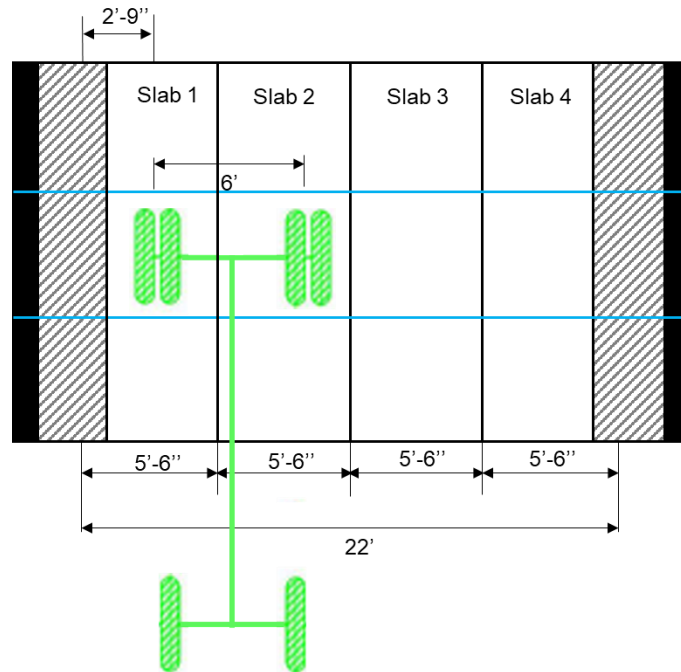


**Figure 3-0-16: H20 truck positions**

In the conventional method of determining load capacity based on Equation 1, certain specifications were taken from the bridge's design documents. These included a concrete strength of 4,000 psi and steel yield strength of 40,000 psi. It was also assumed that the concrete cover is 1.5 inches thick and has a density of 150 pcf, considering the steel reinforcement. The bridge was assumed to have thirteen No. 7 steel bars in the longitudinal direction. Using these assumptions, a resistance value of 172 ft-kips was calculated. The permanent load effect  $Dc$  was calculated to be 17.9 ft-kips. The live load effect ( $L_{FE}$  value) was calculated to be 60 ft-kips. Other standard factors such as the permanent load factor  $\gamma_{DC}$ , the live load factor  $\gamma_L$ , the health condition  $\phi_C$ , the LRFD resistance factor  $\phi$  were respectively set as 1.25, 1.75, 0.85, and 0.9. By considering all the parameters mentioned above, the load rating factor obtained by the conventional method is 0.78.

In contrast, an updated digital twins method was employed, using lab data from an 8.25-inch thick slab. The lab test showed a moment capacity of 253 ft-kips, which was higher than predicted using the conventional assumptions. Although detailed testing was not performed due to budget limits, sample tests from comparable slabs suggested higher material properties. For the digital twins approach, two assumptions were made. Assumption 1 made the adjustment to the concrete strength of 5,000 psi and steel yield strength of 50,000 psi, along with a 1.0-inch concrete cover and thirteen No. 8 bars as longitudinal reinforcement. Using these parameters for the 9.25-inch slab in the Abbeville Bridge led to a resistance value of 290 ft-kips. The load rating factor derived from this assumption is 1.62. However, these estimates might be optimistic, as they differ from the design documents, which specify No. 7 bars. A recalculation using No. 7 rebar was used in Assumption 2 with a resistance value of 231 ft-kip. The load rating factor derived from this assumption is 1.27. additional elements such as the live load effect (LFE value) and the dead

load factor were taken into account. The Finite Element (FE) model revealed that the live load distribution effect is marginally lower compared to the conventional method. Conversely, the dead load impact is effectively captured in the digital twins method, leading to its exclusion from further consideration. Comparative load rating values obtained from both the traditional and digital twins methodologies. The results show that the load rating factors derived using the method are higher than those derived from the traditional method. This suggests that the traditional method may be slightly conservative and could potentially lead to unnecessary load labeling and strengthening of bridges that might otherwise be considered structurally adequate.

### 1.11 Integrating the load rating procedure assisted by digital twin with IBM Maximo

IBM Maximo is a suite of enterprise asset management (EAM) software focused on managing assets, work orders, inventory, and maintenance schedules (IBM., 2023). It provides asset lifecycle and maintenance management for many asset types, including manufacturing, facilities, transportation, and IT assets, etc. Maximo is designed to improve operational efficiency, maximize return on assets, and adhere to compliance standards.

Integrating the load rating procedure assisted by digital twin with IBM Maximo can be helpful in refining the bridge load rating process. Traditional bridge load rating calculations typically rely on static, idealized models and assumptions that fail to account for real-world variables such as material degradation, real-time traffic loads and environmental conditions. In contrast, the digital twin approach incorporates real-time sensor data from fiber optics, strain gauges into finite element simulations. This approach provides a more dynamic and accurate assessment of the current load carrying capacity of bridges. By integrating the load rating procedure assisted by digital into IBM Maximo existing modules, the ability of the software to determine bridge load ratings can be significantly enhanced. For example, the digital twin can utilize real-time stress and strain data to automatically adjust the load rating, triggering appropriate work orders or alarms if readings exceed predefined thresholds. This would make bridge maintenance more dynamic and responsive, moving away from static load rating scales that are infrequently updated.

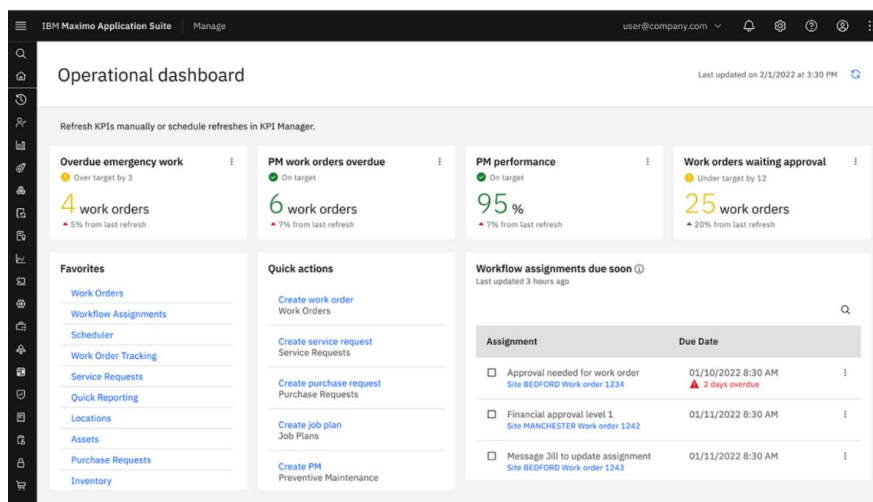


Figure 3-0-17: Operational dashboard of IBM Maximo (IBM 2023)

The integration of digital twin into IBM Maximo not only improves the accuracy of bridge load ratings, but also allows for more efficient allocation of maintenance resources, as work orders can be placed based on real-time demand rather than program estimates (as shown in the image above, IBM Maximo is being updated and managed in real-time for maintenance work orders). As a result, integrating the digital twin approach into IBM Maximo can significantly improve current bridge load rating practices by making bridge load ratings more dynamic, accurate, and responsive to real-world conditions. This has the potential to extend the useful life of bridge assets and allocate maintenance resources more efficiently, although further empirical research is needed to validate these claims.

## Conclusions

This project developed a digital twin load rating method. This method offers an alternative way for load rating evaluations of flat slab bridges. The development of the digital twin integrated laboratory experimental research, field monitoring, and numerical simulations.

Conclusions are summarized as follows:

- By conducting drone inspection and using the pre-trained CNN model, It is possible to estimate the spacing of the cracks and obtain the condition state of the slab which facilitates the determination of the condition factor that can be used to obtain uniform and consistent load rating results.
- The overall accuracy of the improved ensemble ANN in predicting vehicle loads is 86.0%; the ANN can be used to determine vehicle loads in floor slabs. However the drawback of the research on the ensemble ANN in this project is that only data from two loading steps were used for training. More load step data should be added to the training dataset in the future.
- The method of load rating using a digital twin was established through experiments and numerical modeling. The model was further calibrated using field monitoring data from the bridge. After implementing the DT method for load rating, the values for rating factor increased. The reason for the increase in the load rating factor is that the live load distribution in the numerical model is slightly less impactful than traditional methods. Meanwhile, in the DT approach, the effects of deadloads have been fully understood and hence, this factor is no longer considered.

Future work includes further implementation of integrating the developed digital twin-assisted load rating methodology into IBM Maximo. In this way, SCDOT can simulate various scenarios, such as different loads or environmental conditions, in the digital twin to predict the actual response of the bridge. Based on the results of the digital twin's load ratings, potential maintenance needs are automatically identified, and maintenance work orders are generated to ensure that the bridge remains in optimal condition.

## References

- AASHTO (2021). Manual for bridge evaluation, 3rd Ed., Washington, D.C., 2021.
- Ai, L., Soltangharaei, V., Bayat, M., Van Tooren, M., & Ziehl, P. (2021a). Detection of impact on aircraft composite structure using machine learning techniques. *Measurement Science and Technology*, 32(8), 084013.
- Ai, L., Soltangharaei, V., Bayat, M., Greer, B., & Ziehl, P. (2021b). Source localization on large-scale canisters for used nuclear fuel storage using optimal number of acoustic emission sensors. *Nuclear Engineering and Design*, 375, 111097.
- Ai, L., Soltangharaei, V., & Ziehl, P. (2021c). Evaluation of ASR in concrete using acoustic emission and deep learning. *Nuclear Engineering and Design*, 380, 111328.
- Benzon, H.H., Chen, X., Belcher, L., Castro, O., Branner, K., & Smit, J. (2022) An Operational Image-Based Digital Twin for Large-Scale Structures. *Applied Sciences*.12(7):3216.
- Febrianto. E., Butler, L., Girolami, M., & Cirak, F. (2022) Digital twinning of self-sensing structures using the statistical finite element method. *Data-Centric Engineering*. 3:e31.
- Feroz, S., & Abu Dabous, S., 2021. Uav-based remote sensing applications for bridge condition assessment. *Remote Sensing*, 13(9), p.1809.
- IBM. (2023). Infrastructure asset management with IBM Maximo Application Suite
- Islam, A. A., Jaroo, A. S., & Li, F. (2015). Bridge load rating using dynamic response. *Journal of Performance of Constructed Facilities*, 29(4), 04014120.
- Lantsoght, E. O., van der Veen, C., de Boer, A., & Hordijk, D. A. (2017b). State-of-the-art on load testing of concrete bridges. *Engineering Structures*, 150, 231-241.
- Lantsoght, E., van der Veen, C., de Boer, A., & Hordijk, D. A. (2017a). Proof load testing of reinforced concrete slab bridges in the Netherlands. *Structural Concrete*, 18(4), 597-606.
- Lei, Z., Zhu, L., Fang, Y., Niu, C., & Zhao, Y. (2022) Fiber Bragg grating smart material and structural health monitoring system based on digital twin drive. *Journal of Nanomaterials*.
- Lin, K., Xu, Y. L., Lu, X., Guan, Z., & Li, J. (2021) Digital twin-based collapse fragility assessment of a long-span cable-stayed bridge under strong earthquakes. *Automation in Construction*. 123:103547.
- Liu, Y., & Bao, Y. (2023) Automatic interpretation of strain distributions measured from distributed fiber optic sensors for crack monitoring. *Measurement*. 211:112629.
- Metni, N., & Hamel, T., 2007. A UAV for bridge inspection: Visual servoing control law with orientation limits. *Automation in construction*, 17(1), pp.3-10.
- Muhit, I., Kawabe, D., Loverdos, D., Liu, B., Yukihiko, Y., Kim, CW., & Sarhosis V. (2023) A framework for digital twinning of masonry arch bridges. In *Eighth International Symposium on Life-Cycle Civil Engineering*. pp. 817-824. Taylor and Francis Group.
- Rojas-Mercedes, N, Erazo, K., & Di Sarno, L. (2022) Seismic fragility curves for a concrete bridge using structural health monitoring and digital twins. *Earthquake and Structures*, 22 (5). pp. 503-515.
- SCDOT (2019), Load Rating Guidance Document

Yoon, S., Lee, S., Kye, S., Kim, I.H., Jung, H.J., & Spencer Jr BF. (2023) Seismic fragility analysis of deteriorated bridge structures employing a UAV inspection-based updated digital twin. *Structural and Multidisciplinary Optimization*. 65(12):346.

Ziehl, P., Cousins, T., Ross, B., & Huynh, N. (2020). Assessment of structural degradation for bridges and culverts (No. FHWA-SC-20-03). South Carolina. Dept. of Transportation. Office of Materials and Research.